IJMMM International Journal of Minerals, Metallurgy and Materials 矿物冶金与材料学报（英文版）

Superhydrophobic and corrosion-resistant siloxane-modified MgAl–LDHs coatings on magnesium alloy prepared under mild conditions

Wenxi Zhang, Zhangzelong Zhuo, Dan Xu, Liang Wu, and Zhihui Xie

Cite this article as:
Wenxi Zhang, Zhangzelong Zhuo, Dan Xu, Liang Wu, and Zhihui Xie, Superhydrophobic and corrosion-resistant siloxane-modified MgAl–LDHs coatings on magnesium alloy prepared under mild conditions, *Int. J. Miner. Metall. Mater.*, 32(2025), No. 2, pp. 450-463. https://doi.org/10.1007/s12613-024-2927-3

Articles you may be interested in

Yahya Jafari Tarzanagh, Davod Seifzadeh, and Roghaye Samadianfard, Combining the 8-hydroxyquinoline intercalated layered double hydroxide film and sol–gel coating for active corrosion protection of the magnesium alloy, *Int. J. Miner. Metall. Mater.*, 29(2022), No. 3, pp. 536-546. https://doi.org/10.1007/s12613-021-2251-0

Jing Han, Cong Wang, Yuanming Song, Zhiyuan Liu, Jiapeng Sun, and Jiyun Zhao, Simultaneously improving mechanical properties and corrosion resistance of as-cast AZ91 Mg alloy by ultrasonic surface rolling, *Int. J. Miner. Metall. Mater.*, 29(2022), No. 8, pp. 1551-1558. https://doi.org/10.1007/s12613-021-2294-2

Hassan Jafari, Amir Houshang Mojiri Tehrani, and Mahsa Heydari, Effect of extrusion process on microstructure and mechanical and corrosion properties of biodegradable Mg–5Zn–1.5Y magnesium alloy, *Int. J. Miner. Metall. Mater.*, 29(2022), No. 3, pp. 490-502. https://doi.org/10.1007/s12613-021-2275-5

Nikhil, Gopal Ji, and Rajiv Prakash, Hydrothermal synthesis of Zn–Mg-based layered double hydroxide coatings for the corrosion protection of copper in chloride and hydroxide media, *Int. J. Miner. Metall. Mater.*, 28(2021), No. 12, pp. 1991-2000. https://doi.org/10.1007/s12613-020-2122-0

Dong Wang, Chen Ma, Jinyu Liu, Weidong Li, Wei Shang, Ning Peng, and Yuqing Wen, Corrosion resistance and anti-soiling performance of micro-arc oxidation/graphene oxide/stearic acid superhydrophobic composite coating on magnesium alloys, *Int. J. Miner. Metall. Mater.*, 30(2023), No. 6, pp. 1128-1139. https://doi.org/10.1007/s12613-023-2596-7

Debasis Saran, Atul Kumar, Sivaiah Bathula, David Klaumünzer, and Kisor K Sahu, Review on the phosphate-based conversion coatings of magnesium and its alloys, *Int. J. Miner. Metall. Mater.*, 29(2022), No. 7, pp. 1435-1452. https://doi.org/10.1007/s12613-022-2419-2

IJMMM WeChat

QQ author group

INTERNATIONAL JOURNAL OF
Minerals, Metallurgy and Materials

Volume 32, Number 2, February 2025
Page 450

Research Article https://doi.org/10.1007/s12613-024-2927-3

Superhydrophobic and corrosion-resistant siloxane-modified MgAl–LDHs coatings on magnesium alloy prepared under mild conditions

Wenxi Zhang[1)], *Zhangzelong Zhuo*[1)], *Dan Xu*[1)], *Liang Wu*[2)], *and Zhihui Xie*[1),✉]

1) Chemical Synthesis and Pollution Control Key Laboratory of Sichuan Province, College of Chemistry and Chemical Engineering, China West Normal University, Nanchong 637002, China

2) College of Materials Science and Engineering/National Engineering Research Center for Magnesium Alloys, Chongqing University, Chongqing 400044, China

(Received: 18 January 2024; revised: 18 April 2024; accepted: 6 May 2024)

Abstract: We have developed a superhydrophobic and corrosion-resistant LDH-W/PFDTMS composite coating on the surface of Mg alloy. This composite comprised a tungstate-intercalated (LDH-W) underlayer that was grown at low temperature (relative to hydrothermal reaction conditions) under atmospheric pressure and an outer polysiloxane layer created from a solution containing perfluorodecyltrimethoxysilane (PFDTMS) using a simple immersion method. The successful intercalation of tungstate into the LDH phase and the following formation of the polysiloxane layer were confirmed through X-ray diffraction (XRD), Fourier transform infrared (FTIR) spectroscopy, and X-ray photoelectron spectroscopy (XPS). The corrosion resistance of the LDH-W film, both before and after the PFDTMS modification, was evaluated using electrochemical impedance spectroscopy (EIS), Tafel curves, and immersion experiments. The results showed that Mg coated with LDH-W/PFDTMS exhibited significantly enhanced corrosion protection compared to the unmodified LDH-W film, with no apparent signs of corrosion after exposure to 3.5wt% NaCl solution for 15 d. Furthermore, the LDH-W/PFDTMS coating demonstrated superior superhydrophobicity and self-cleaning properties against water and several common beverages, as confirmed by static contact angle and water-repellency tests. These results offer valuable insights into preparing superhydrophobic and corrosion-resistant LDH-based composite coatings on Mg alloy surfaces under relatively mild reaction conditions.

Keywords: Mg alloy; corrosion; coating; layered double hydroxide

1. Introduction

Mg alloys are notable for their excellent physicochemical properties, making them popular in various industries, including automotive [1–2], aerospace [3–5], electronics [6–7], and biomedical [1–3]. Despite their advantages, their low corrosion potentials (−1.5 V vs. SHE (standard hydrogen electrode)) render them highly susceptible to corrosion, limiting their wider application. Designing suitable surface coatings is an effective way to suppress corrosion. Common surface treatments for Mg alloys mainly include chemical conversion films [4–8], metal plating [9–11], micro-arc oxidation [12–17], and organic coatings [18–20]. Among these, layered double hydroxides (LDHs) have attracted much attention recently owing to their environmental friendliness, low cost, and simple preparation process, positioning them as potential alternatives to traditional, carcinogenic chromate coatings. However, LDH layers inherently contain micro/nanopores that can act as diffusion channels for aqueous corrosive agents, thereby requiring appropriate post-treatment to enhance corrosion resistance. A typical method involves the deposition of additional layers onto the LDH surface to fill and seal these pores. For example, Ni–P alloys have been used to fill the porous structure of the LDH film, while organic layers have been applied to cover the microdefects on the LDH surface [21–22].

Superhydrophobic surfaces offer an effective method for improving corrosion protection through their outstanding self-cleaning and water-repellency capabilities, which prolong the penetration of corrosive media to the metal substrate [23–24]. Typical superhydrophobic coatings exhibit micro/nanorough structures with a low surface energy [25]. Although numerous methods for preparing such coatings have been reported, most emphasize the micro/nanorough structure and low surface energy. For example, composite coatings prepared by spraying SiO_2-modified polydimethylsiloxane on the microarc oxidized coating have demonstrated sustained superhydrophobicity in acid, alkali, high/low temperature, and UV radiation exposure, leading to impressive corrosion resistance in neutral solutions [26]. Another approach involved the development of dodecyltrimethoxysilane-modified $Mg(OH)_2$ superhydrophobic coating through electrodeposition, reaching a contact angle of (165.1 ± 2.1)° and decreasing the corrosion current density by three orders of magnitude compared to that of the uncoated AZ31 Mg alloy [27]. The LDH film comprises many perpendicu-

✉ Corresponding author: Zhihui Xie E-mail: zhxie@cwnu.edu.cn

larly grown nanosheets and exhibits a micro/nanoscale rough structure. The post-treatment process for pore closure should mainly focus on imparting low surface energy to the coating. Silanization is a low-cost and effective method for achieving low surface energies in coatings. During this process, silanol groups (Si–OH) generated by the hydrolysis of fluorosilanes condense with hydroxyl groups (metal–OH) on the metal surface, leading to the formation of Me–O–Si bonds. Meanwhile, dehydration polymerization between Si–OH generates Si–O–Si bonds, forming chemically stable and corrosion-resistant polysiloxane films [28]. The LDH coating, rich in hydroxyl groups (–OH), benefits from the condensation reaction facilitated by silane treatment on its surface, promoting the development of superhydrophobic coating with strong adhesion [29].

Most of the existing literature on preparing corrosion-resistant LDH films on Mg alloys uses hydrothermal methods that require high temperatures and pressures. In this study, we first developed a tungstate-intercalated MgAl–LDH film on the surface of Mg alloy with the assistance of a chelator under relatively mild conditions. This was followed by a modification of the LDH phase using perfluorodecyltrimethoxysilane (PFDTMS) as low-surface-energy substance to produce LDH-W/PFDTMS composite coating. The successful incorporation of PFDTMS into the LDH layer was confirmed by characterizing the composite coating's surface morphology, composition, and structure. Electrochemical measurements, immersion experiments, and contact angle tests showed that the LDH-based coatings, modified by the siloxane film, greatly improved the corrosion resistance of the Mg alloy and exhibited superior superhydrophobicity and self-cleaning capabilities.

2. Experimental

2.1. Reagents and materials

The composition of the AZ31 Mg alloy sheet (30 mm × 20 mm × 2.0 mm) includes 2.75wt% Al, 1.15wt% Zn, 0.16wt% Mn, and the remainder Mg. The chemical reagents, including ethylenediaminetetraacetic acid (EDTA, 98%), sodium hydroxide (NaOH, 98%), sodium chloride (NaCl, >99%), sodium tungstate (Na_2WO_4, 98%), sodium nitrate ($NaNO_3$, AR), and 1H, 1H, 2H, 2H-perfluorodecyltrimethoxysilane (PFDTMS, ≥97%) were purchased from Aladdin Industrial Corporation. Deionized water with resistance of 18.2 MΩ·cm at 25°C was prepared using water purification system (UPT-II-10T)

2.2. Coating preparation

2.2.1. Preparation of LDH film

The aqueous solution containing the chelating agent EDTA (0.1 mol/L) and sodium nitrate (0.25 mol/L) was prepared. The pH value of the solution was adjusted to (10.0 ± 0.1) using NaOH solution (0.5 mol/L). Under continuous stirring, a polished AZ31 specimen was immersed into the solution (200 mL) and reacted for 12 h at (95 ± 1)°C.

2.2.2. Preparation of inhibitor-intercalated LDH film

The pH of Na_2WO_4 (0.1 mol/L) solution was adjusted to (10.0 ± 0.1) using 0.1 mol/L NaOH aqueous solution. Under continuous stirring, the LDH-coated Mg alloy was immersed into the inhibitor solution for an ion-exchange reaction for 4 h at 95°C. After the anion exchange treatment, the sample was washed with deionized water, dried in air, and named LDH-W.

2.2.3. Preparation of LDH-W/PFDTMS coating

The LDH-W samples were immersed in 50:50 (*V*/*V*) mixture of CH_3CH_2OH and H_2O containing PFDTMS (0.1 M) for modification at ambient temperature and atmospheric pressure for 12, 18, 24, and 30 h, respectively. The modified samples were washed thoroughly with ethanol and deionized water and dried in an oven at 60°C for 2 h. The resulting samples were labeled LDH-W/PFDTMS-*x* (*x* = 12, 18, 24, and 30 h). According to Scheme 1, the preparation of the LDH coating occurred at relatively low temperature under atmospheric pressure. This led to the incomplete transformation of the $Mg(OH)_2$ phase on the surface of the Mg alloy into the LDH phase, resulting in the formation of thin $Mg(OH)_2$ film underneath the LDH layer.

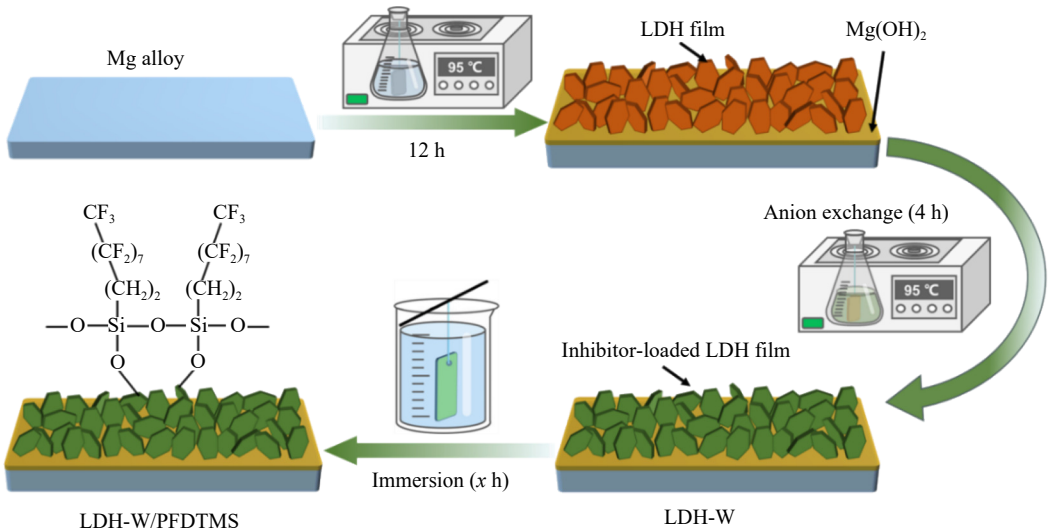

Scheme 1. Schematic of LDH-W/PFDTMS composite coating on Mg alloy surface.

2.3. Characterization and electrochemical measurements

Scanning electron microscope (SEM, Hitachi SU8020) was used to observe the surface morphology and microstructure of the LDH-W and LDH-W/PFDTMS coatings. The elemental composition of the coatings was characterized by energy dispersive spectroscopy (EDS). The functional groups on the coating surface were analyzed using Fourier transform infrared spectroscopy (FTIR, Nicolet-6700, USA, wavenumber range: 500–4000 cm^{-1}). The crystallographic features of both LDH and LDH-W coatings were characterized using X-ray diffraction (XRD, D8 ADVANCE, Germany), with the measurements carried out at a scanning speed of $5°\cdot min^{-1}$ in the 5°–80° range at voltage of 40 kV and current of 30 mA. The compositions of the LDH-W and LDH-W/PFDTMS coatings were also determined by X-ray photoelectron spectroscopy (XPS, 250Xi, Thermo-escalab, Waltham, MA, USA). The acquired XPS data were analyzed using XPS peak software. The coatings' surface roughness (R_a) values were measured using a 3D profilometer (Contour GT-X, Germany). Their static contact angles (CAs) were recorded using an optical contact angle meter (SL200KS, KINO, USA) at 25°C with a droplet volume of 5.0 μL. These measurements were performed by determining and averaging the water CA values at five different points on the coating surface to ensure reproducibility.

The electrochemical impedance spectroscopy (EIS) and Tafel curves of the samples were obtained by electrochemical workstation (Gamry, USA) to assess the corrosion resistance. A custom-designed set-up featuring a three-electrode system was used for the electrochemical test. The samples (Mg alloy, LDH-W, or LDH-W/PFDTMS-x coating) with exposed area of 1.0 cm^2 served as the working electrode, with a platinum (Pt) sheet and a saturated calomel electrode (SCE) acting as the counter and reference electrodes, respectively. To shield against external electromagnetic interference, the three-electrode system was placed within a Faraday cage. Before collecting EIS and Tafel data, the system was immersed in a corrosive solution for over 20 min until the open circuit potential (OCP) was stabilized. EIS measurements were performed in the frequency range of 10^5–10^{-2} Hz with a perturbation potential of 5.0 mV. The EIS data was fitted using different equivalent circuit diagram (EC) models through Gamry Analyst software. The Tafel curves were obtained in the potential range of −300–300 mV (vs. OCP) at a scanning rate of 1.0 $mV\cdot s^{-1}$. All electrochemical experiments were repeated at least three times.

3. Results and discussion

3.1. Surface morphology and composition of the LDH-W and LDH-W/PFDTMS coatings

The surface morphologies of the LDH-W films before and after PFDTMS modification are shown in Fig. 1. A noticeable change in the surface morphology of the LDH film before and after modification is not observed (Fig. 1(a)–(c) and (e)–(g)). Both LDH coatings display a typical LDH nanosheet structure, indicating that the siloxane modification does not change the surface structure. After analyzing the chemical compositions of the LDH-W and LDH-W/PFDTMS coating surfaces (Fig. 1(c) and (f)), only Mg, Al, O, C, N, and W elements are detected on the surface of the LDH-W coating. By contrast, in addition to these elements in the LDH-W film, abundant F and Si elements are identified on the LDH-W/PFDTMS coating surface after PFDTMS modification. The contents of the Mg and Al elements on the surface of the LDH-W/PFDTMS coating are significantly reduced, while the content of the C element is significantly increased from 5.52wt% to 26.4wt% (Table 1). This elemental change preliminarily indicates the successful generation of polysiloxane film on the LDH-W layer surface.

The XRD patterns of the LDH and LDH-W films grown on Mg alloys are shown in Fig. 2(a). They highlight the characteristic diffraction peaks of the (006) and (003) crystal planes of the LDH phase without inhibitor, located at diffraction angles (2θ) of 23.3° and 11.6°, respectively. This pattern suggests that the interlayer anions of the LDH film prepared using EDTA solution are CO_3^{2-} or NO_3^- [30]. After treatment with an inhibitor (resulting in LDH-W), these characteristic diffraction peaks shifted to 22.7° and 11.2°, respectively [31].

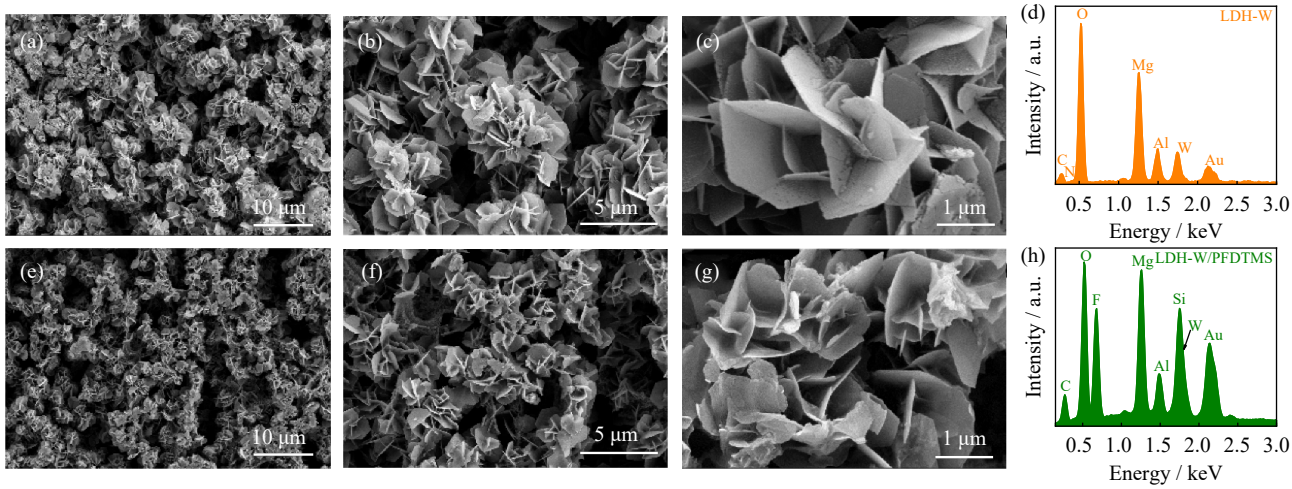

Fig. 1. SEM images and EDS spectra of (a–d) LDH-W and (e–h) LDH-W/PFDTMS coatings on the Mg alloy.

Table 1. Surface EDS composition of the LDH-W and LDH-W/PFDTMS coatings on the Mg alloy wt%

Samples	Mg	Al	C	O	N	W	F	Si
LDH-W	23.87	8.53	5.52	48.02	0.67	13.38	—	—
LDH-W/ PFDTMS	10.80	3.60	26.40	23.80	0.20	1.20	29.5	4.4

This shift is attributed to a slight increase in the interlamellar distance as a consequence of the inhibitor anions being intercalated into the LDH interlayers [32]. The FTIR spectra of the LDH-W composite coatings before and after the PFDTMS modification are presented in Fig. 2(b). The FTIR spectra show that the chemical groups in the LDH-W coating mainly include hydroxyl groups (–OH) (3520 and 1650 cm^{-1}) [33–34], C–O (1430 and 1010 cm^{-1}), and W–O–W (858 cm^{-1}) [35]. Two additional absorption peaks appear at 1150 and 1210 cm^{-1} in the FTIR spectra of the LDH-W/PFDTMS coating, attributed to the Si–O and C–F bonds [29]. The results confirm the successful formation of polysiloxane on the LDH-W film surface.

The composition and elemental chemical state at the surface of the LDH-W and LDH-W/PFDTMS coatings were determined using XPS. For the LDH-W film, the C 1s profile consists mainly of two peaks located at 284.9 and 288.3 eV (Fig. 3(a)), which are attributed to the contaminated carbon and O=C–O bond from the CO_3^{2-} in the LDH phase, respectively [29]. Following PFDTMS modification, the LDH-W/PFDTMS coating surface mainly contains C, F, O, and Si. The C 1s spectrum was deconvoluted into four peaks, including two characteristic peaks (C–C and C=O–C) associated with the LDH-W phase and two characteristic peaks of 291.3 and 293.4 eV, corresponding to $–CF_2–$ and $–CF_3$, respectively [36]. These findings further confirm the existence of polysiloxane film in the LDH phase. This conclusion is further supported by the high-resolution XPS spectra of the O 1s, F 1s, and Si 2p. The three fitted peaks in the O 1s spectrum of the LDH-W coating correspond to W–O (530.2 eV), M–OH (531.5 eV), and intercalated H_2O molecules (532.3 eV) (Fig. 3(b)) [37–39]. In addition, a characteristic peak of the Si–O bond is observed at 532.9 eV in the high-resolution XPS spectra of the PFDTMS-modified sample [40]. The F 1s and Si 2p high-resolution XPS spectra of the LDH-W/PFDTMS coating exhibit obvious characteristic peaks originating from the F–C (687.7 eV) and Si–O (102.7 eV) bonds, respectively (Fig. 3(c) and (d)) [41–42]. Typically, the average depth of XPS analysis is less than 10 nm, allowing for the detection of chemical elements in the underlying LDH layer unless the top layer is very thin. Conversely, if the surface layer is too thick, detecting elements in the bottom layer becomes challenging. This suggests that the thickness of the formed polysiloxane film is likely only a few nanometers.

The cross-sectional SEM image and EDS maps of the LDH-W/PFDTMS composite coating are presented in Fig. 4. This cross-sectional view reveals four distinct regions from top to bottom, corresponding to the polysiloxane, LDH, $Mg(OH)_2$ films, and the magnesium alloy substrate, respectively. The polysiloxane film mainly comprises C, F, and Si elements, while the $Mg(OH)_2$ film consists of Mg and O elements. In addition to the two elements, the LDH film comprises Al, C, W, and Si elements. Based on the cross-sectional SEM image and the distribution of Mg in the bottom region, the total thickness of the composite coating is estimated to be approximately 34.5 μm. The presence of Al in the LDH phase, but not in the $Mg(OH)_2$ layer, allows for the differentiation between the thicknesses of the LDH and $Mg(OH)_2$ layers, measured at 23.2 and 11.3 μm, respectively. The detection of a small amount of Al outside the $Mg(OH)_2$ layer is attributed to the diffusion of different elements during sample preparation. The latter involved a mechanical polishing machine with running water. Similar diffusion phenomena are observed for the W, F, and Si elements.

3.2. Superhydrophobicity, self-cleaning, water repellency and surface roughness of the LDH-W/PFDTMS coating

Wettability significantly affects the corrosion resistance of coatings on Mg alloy surfaces. Fig. 5 illustrates the changes in water CA (WCA) values for LDH-W-based coatings immersed in PFDTMS solution over different durations. The WCA value of the untreated LDH-W coating is only (13.3 ± 0.3)°, indicating a hydrophilic state owing to the large number of hydrophilic –OH groups in the LDH phase. All PFDTMS-modified LDH-W samples exhibit superhydrophobicity. The WCA values of the LDH-W coatings after immer-

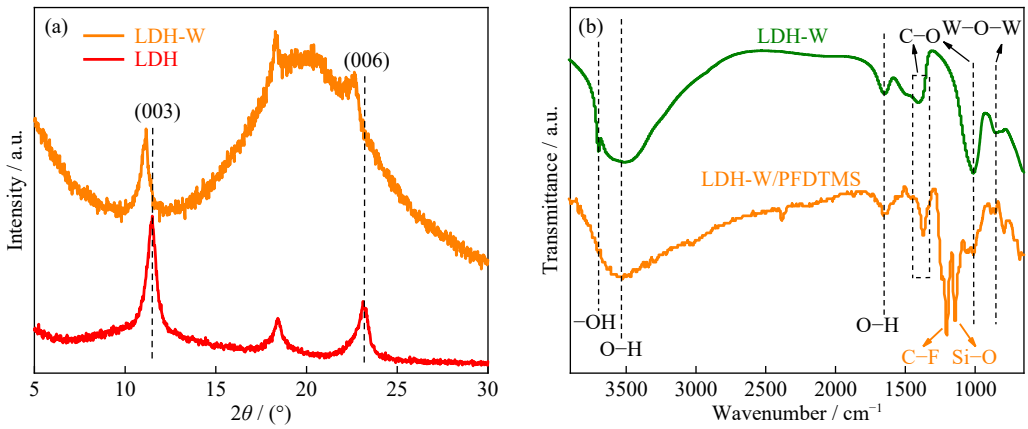

Fig. 2. (a) XRD patterns and (b) FTIR spectra of different LDH-based films on the Mg alloy.

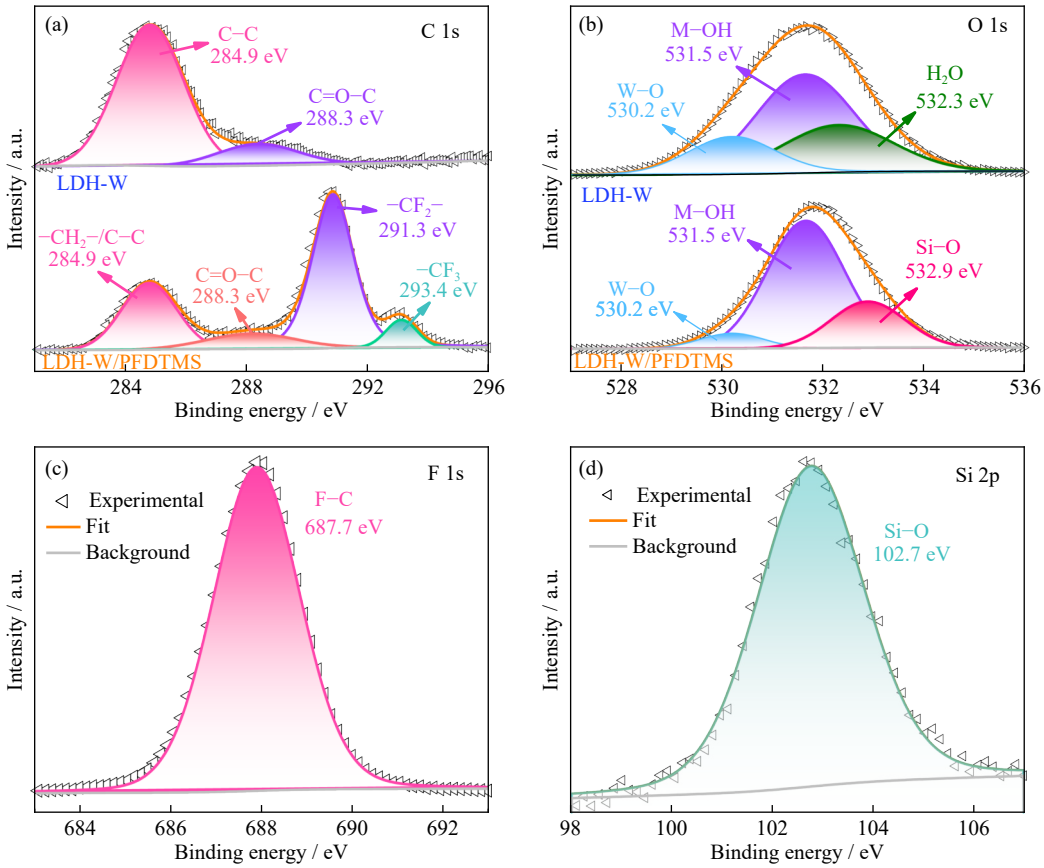

Fig. 3. High-resolution XPS spectra of (a) C 1s, (b) O 1s, (c) F 1s, and (d) Si 2p of the LDH-W coating and LDH-W/PFDTMS coating.

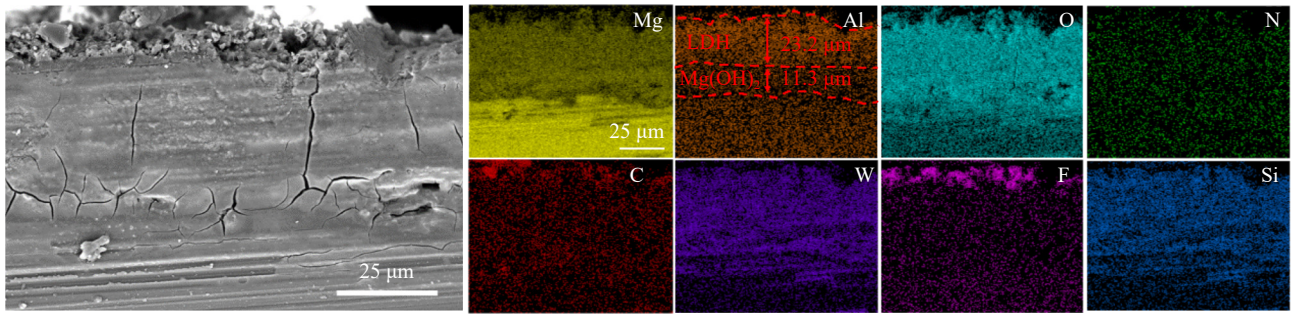

Fig. 4. Cross-sectional SEM images and corresponding EDS maps at the surface of the composite coating on the Mg alloy.

sion in PFDTMS solution for 12 and 18 h are (150.5 ± 2.2)° and (155.6 ± 1.6)°, respectively. This significant increase in WCA indicates the shift from hydrophilicity to superhydrophobicity on the surface of the LDH-W coating following PFDTMS treatment. Extending the immersion time to 24 h allows for sufficient reaction between the silanol in the siloxane with the hydroxyl groups on the LDH film surface, resulting in a remarkable increase in WCA to (162.2 ± 1.7)°. Further increasing the immersion time to 30 h causes the WCA value of the composite coating to decrease to (156.8 ± 2.4)° (Fig. 5(e)). The slight decrease in WCA may attributed to the formation of an excess amount of polysiloxane film, which, in turn, reduces the surface roughness [43]. Therefore, a 24-h immersion period is identified as the optimal duration for PFDTMS treatment of LDH-W coatings.

The Wenzel model can explain the lower WCA values of

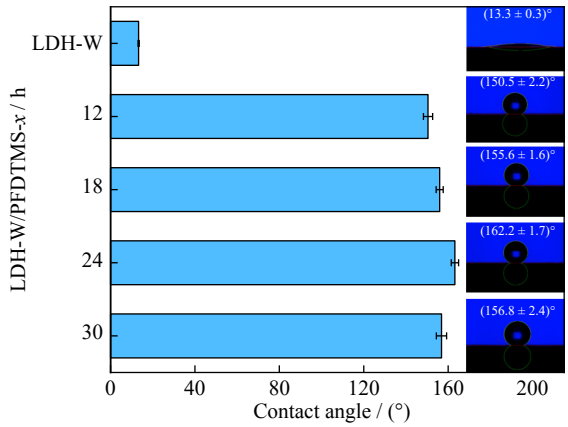

Fig. 5. Water static contact angles for LDH-W and LDH-W/PFDTMS-*x* (*x* = 12, 18, 24, 30 h) coatings.

the LDH-W coating compared to the bare Mg alloy (46.2 ± 2.2)° [26,44–45]. According to the Wenzel equation:

$$\cos\theta_1 = r\cos\theta \quad (1)$$

where θ is the intrinsic CA on an ideally smooth surface, r is the roughness factor, and θ_1 denotes the apparent CA on a rough surface, equivalent to the static CA values measured. When $\theta > 90°$ (indicating hydrophobic surface), θ_1 increases with increasing r, suggesting that the rougher the solid surface, the more hydrophobic it becomes. Conversely, when $\theta < 90°$ (signifying hydrophilic surface), θ_1 decreases with increasing r, meaning that the rougher the solid surface, the more hydrophilic it appears [46]. The bare Mg alloy surface is prone to oxidization, leading to the formation of a corrosive film enriched with hydroxyl groups, thereby presenting a hydrophilic state. Similarly, the LDH-W film is abundant in hydroxyl groups and exhibits hydrophilicity. Moreover, its surface roughness significantly exceeds that of the bare Mg alloy, resulting in enhanced hydrophilicity as reflected by smaller WCA of (13.3 ± 0.3)°. This increased hydrophilicity allows water and corrosive media to fully saturate the entire surface of the LDH film and fill these gaps among the nanosheets. Consequently, this wettability accelerates the penetration of aqueous corrosive media through the micro and nanopores into the LDH, reaching the Mg alloy substrate beneath, which negatively affects corrosion protection.

The polysiloxane film formed on the LDH-W surface contains hydrophobic groups such as $–CF_2–$, $–CF_3$, and $–CH_2–$ groups after PFDTMS treatment, which reduces the surface free energy and repels –OH groups. This transformation shifts the surface from hydrophilic to hydrophobic. Consequently, the nanosheets and air trapped among the LDH-W nanosheets act as a cushion, preventing the aqueous corrosive solution from fully impregnating the surface, thereby reducing the corrosion rate. The polysiloxane content increases as modification time rises, enhancing hydrophobicity and achieving the highest WCA value of (162.2 ± 1.7)°. The Cassie–Baxter model elucidates the decline in the WCA value of the composite coating with excess modification time. According to the Cassie–Baxter equation:

$$\cos\theta_{CB} = f(\cos\theta + 1) - 1 \quad (2)$$

where θ_{CB} represents the apparent CA on the solid surface (i.e., the measured static CA), and f is the contact fraction at the solid–liquid interface. The θ_{CB} increases as the f decreases until approaching 180° when the latter approaches 0 [47–48]. A long modification time causes the formation of an excessively thick polysiloxane film on the LDH-W surface, which increases the contact fraction f of the solid–liquid interface, which, in turn, lowers the θ_{CB} value [28]. This decreased hydrophobicity adversely affects the coating's corrosion resistance. Hereafter, LDH-W/PFDTMS denotes the LDH-W layer treated with PFDTMS for 24 h.

The wettability result of several common liquids, including NaCl solution, cola, milk, coffee, and tea drops, on the LDH-W/PFDTMS surface, are shown in Fig. 6. All liquid drops form near-spherical shapes on the composite coating surface, with CAs exceeding 150°. These results demonstrate the LDH-W/PFDTMS coating's excellent ability to repel commonly encountered liquids. In particular, the CA value reaches 160.9° for a corrosive solution containing Cl^-.

The self-cleaning capabilities were evaluated by placing the LDH-W and LDH-W/PFDTMS coatings in Petri dishes at angles of less than 10° to the horizontal plane. Graphite powder was used as a contaminant, randomly scattered on the coating surfaces, followed by rinsing with water droplets. For the LDH-W coating, water droplets contacted the surface and then immediately spread out and wetted the coating surface (Fig. 7(a) and (b)). The surface became completely wet as more water drops fell. After rinsing, most of the graphite powder was removed with the water droplets under the force of gravity, leaving only a small portion on the surface, which then accumulated at the lower edge of the sample. By contrast, the water droplets on the surface of the LDH-W/PFDTMS coating demonstrated different behavior (Fig. 7(d) and (e)). Water droplets remained spherical and flowed rapidly along the inclined surface toward the Petri dish, carrying the graphite powder quickly into the dish. After rinsing, the sample surface remained dry and clean, with no visible residual graphite powder. A water-repellency test further verified the superior hydrophobicity and lower water adhesion of the LDH-W/PFDTMS composite coating compared to the LDH-W coating. The sample was horizontally fixed using an elec-

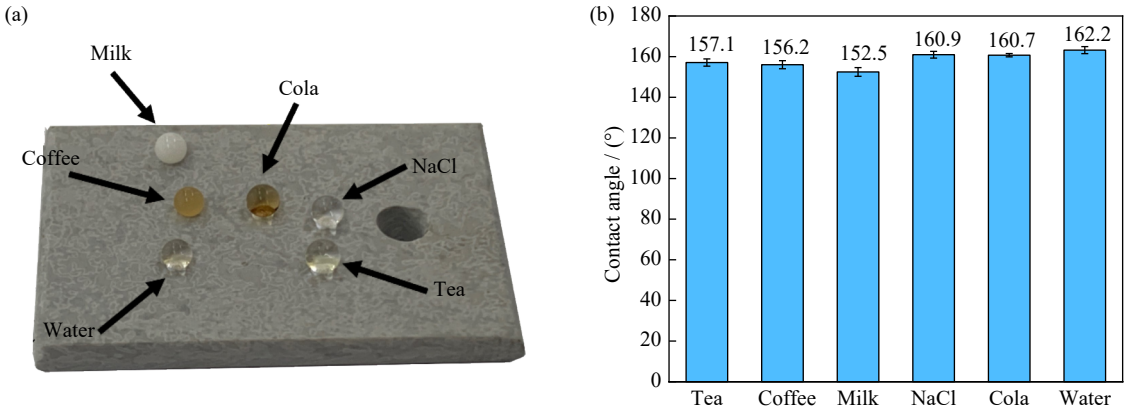

Fig. 6. (a) Digital images of tea, coffee, milk, cola, water, and NaCl solution droplets on the surface of the LDH-W/PFDTMS-24 h coating and (b) corresponding static contact angle histograms.

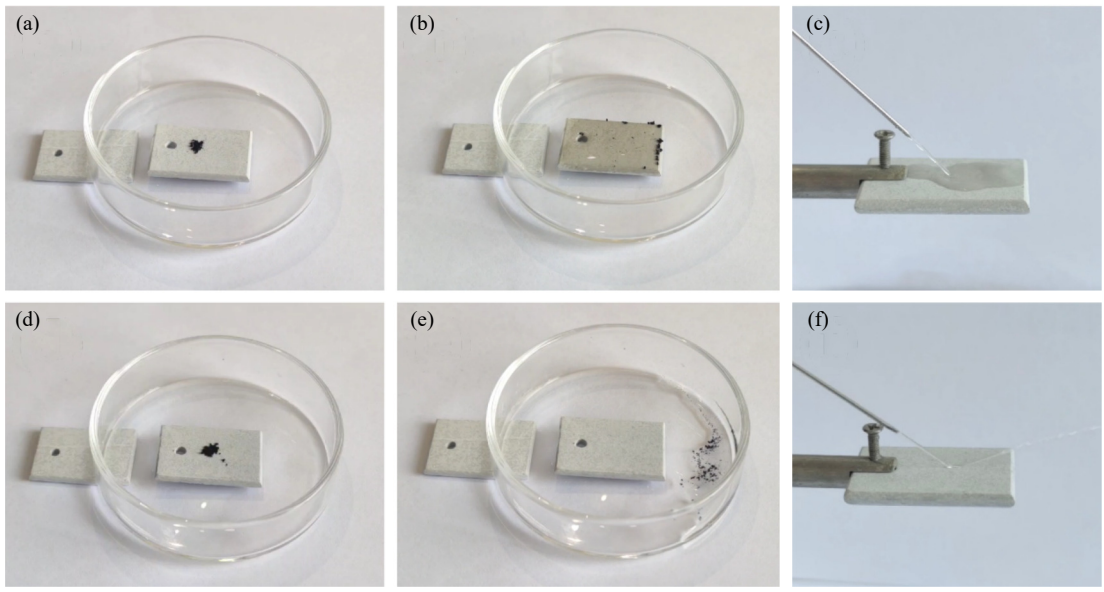

Fig. 7. (a, b, d, e) Self-cleaning and (c, f) water-repellency tests of LDH-W and LDH-W/PFDTMS coatings, respectively.

trode clamp, and a needle was used to spray water column onto the sample surface. The water immediately spread on the surface of the LDH-W coating when the water column contacted the surface (Fig. 7(c)), manifesting strong hydrophilicity. By contrast, the water column was instantly ejected away from the surface of the LDH-W/PFDTMS coating (Fig. 7(f)), with no water stains or droplet spreading observed, demonstrating its exceptional water-repellency ability.

The roughness of the LDH-W coating surface before and after PFDTMS treatment was assessed using three-dimensional profilometer (Fig. 8(a) and (b)). Both coatings presented similar micro/nanosized peaks and comparable roughness (R_a) levels, indicating negligible changes in the surface microstructure of the coating after being modified by PFDTMS, consistent with the SEM image result. The exceptional superhydrophobic performance of the composite coating is attributed to its micro/nanoscale rough structure combined with low surface energy. The WCA value of the LDH-W/PFDTMS coating decreased evidently to (150.2 ± 1.9)° after 15 d of exposure to neutral corrosive solution but remained superhydrophobic. After four months of exposure to air, the WCA value decreases by only 2.7° to (159.5 ± 2.1)°, maintaining high hydrophobicity (Fig. 8(c) and (d)).

3.3. Corrosion resistance of the LDH-W and LDH-W/PFDTMS coatings

The effect of immersion time in PFDTMS solution on the EIS plots and Tafel curves of the LDH-W/PFDTMS-*x* coating, along with the fitted electrochemical parameters based on the EC model, is illustrated in Fig. 9 and Table 2. In general, a higher impedance modulus in the low-frequency region of the EIS spectrum indicates better corrosion resistance of the coating [49–50]. This varied corrosion resistance was also confirmed by the diameter of the capacitance arc in the Nyquist diagram (Fig. 9(c)), where larger diameter denotes

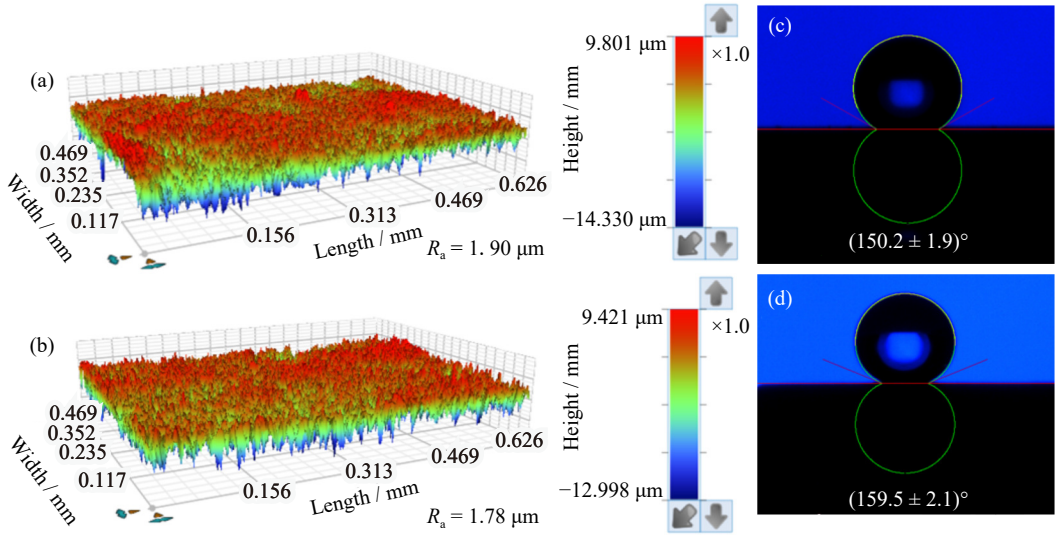

Fig. 8. 3D surface roughness maps of the (a) LDH-W and (b) LDH-W/PFDTMS coatings. Static contact angles of the latter after (c) 15 d of immersion in 3.5wt% NaCl solution and (d) 4 months of exposure to air.

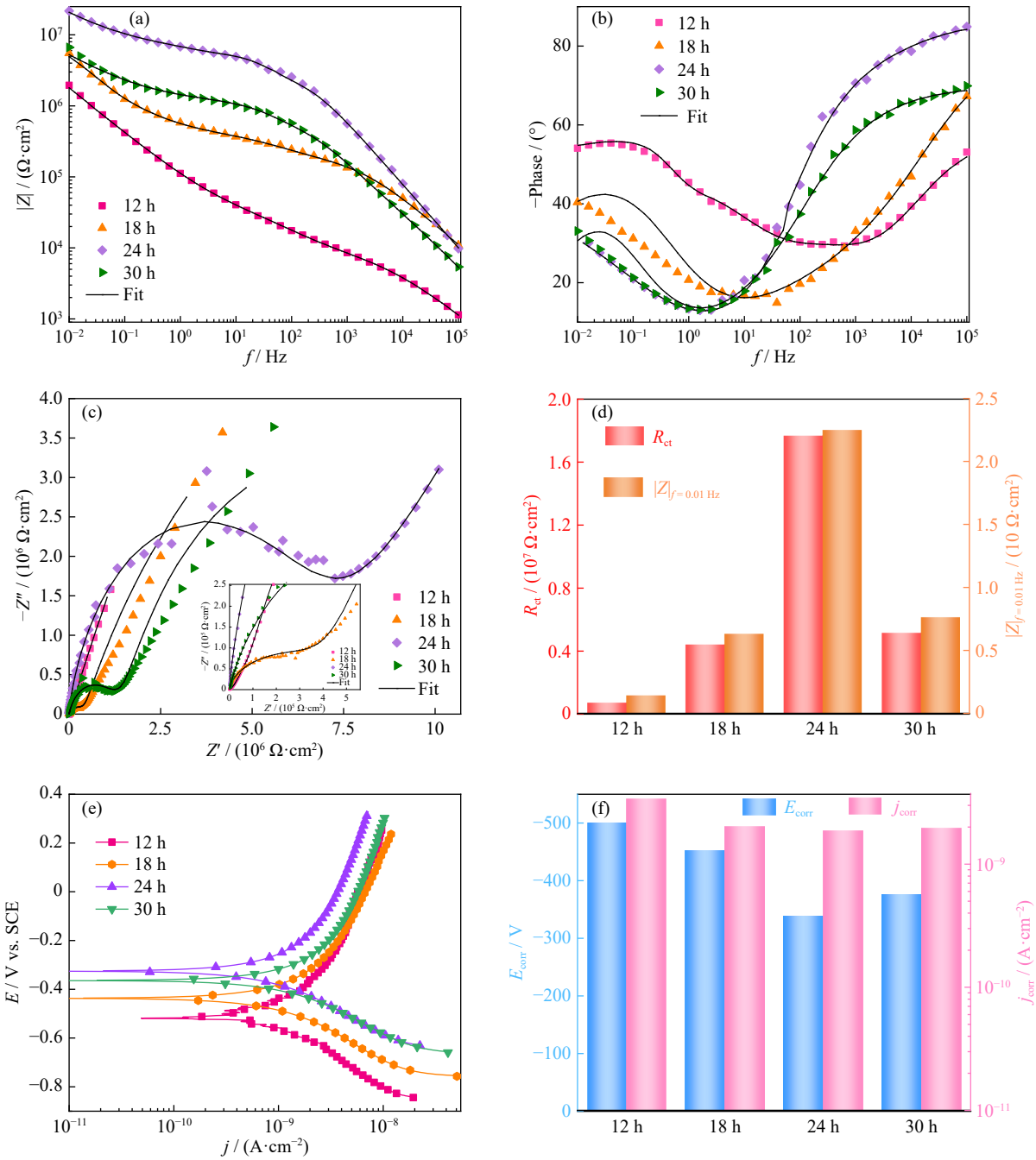

Fig. 9. (a) Bode magnitude diagrams, (b) Bode phase diagrams, (c) Nyquist diagrams, (d) corresponding histograms for R_{ct} and $|Z|_{f=0.01\ Hz}$, (e) Tafel curves, and (f) corresponding histograms for E_{corr} and j_{corr} of the LDH-W/PFDTMS-*x* coating.

Table 2. Fitted EIS parameters for LDH-W/PFDTMS-*x* coatings

LDH-W/PFDTMS-*x*	$\|Z\|_{f=0.01\ Hz}$ / (Ω·cm²)	R_s / (Ω·cm²)	Y_{PFDTMS} / (10^{-9} S·s^n·cm^{-2})	R_{PFDTMS} / (kΩ·cm²)	Y_{LDH} / (10^{-9} S·s^n·cm^{-2})	R_{LDH} / (kΩ·cm²)	Y_c / (10^{-9} S·s^n·cm^{-2})	R_c / (kΩ·cm²)	Z_W / (10^{-5} S·s$^{0.5}$·cm^{-2})	Y_{dl} / (10^{-9} S·s^n·cm^{-2})	R_{ct} / (kΩ·cm²)	χ^2 / 10^{-3}
12 h	1.22×10^6	4.6	8.97	503	8.99	3898	14.63	3012	5.6	9.84	875	5.4
18 h	5.48×10^6	8.2	8.25	863	7.92	4020	13.40	3250	7.1	7.51	5100	2.4
24 h	2.20×10^7	5.6	5.73	3750	3.57	5800	9.74	3500	8.7	5.83	18000	1.8
30 h	6.40×10^6	6.8	6.59	1193	5.77	4640	10.21	3220	6.5	6.77	6150	4.9

enhanced corrosion resistance [51]. The LDH-W/PFDTMS-24 h coating exhibited exceptional corrosion resistance. The higher the corrosion potential (E_{corr}) and the lower the corrosion current density (j_{corr}) in the Tafel curve, the better the corrosion resistance of the coating [52]. The low-frequency impedance modulus of the LDH-W/PFDTMS-*x* coating increases and then decreases with increasing immersion time (Fig. 9(a) and (d)). The impedance modulus value of the

composite coating peaks at modification time of 24 h (up to 18 MΩ·cm^2). The E_{corr} of the sample shifts positively, and the j_{corr} gradually decreases as the reaction time increases from 12 to 24 h (Fig. 9(e) and (f) and Table 3). Extending the modification time further to 30 h results in a decrease in E_{corr} and an increase in j_{corr}; the corrosion potential of the LDH-W/PFDTMS-24 h coating is −338 mV, and the corrosion current density is 1.86 × 10^{-9} A·cm^{-2}. These electrochemical tests indicate the optimal corrosion resistance offered by the LDH-W/PFDTMS-24 h coating. The reduced corrosion resistance of the LDH-W coating with overly prolonged PFDTMS treatment may be attributed to a decrease in hydrophobicity, as previously discussed.

Fig. 10 displays the EIS spectra and Tafel curves for Mg alloy, LDH-W, and LDH-W/PFDTMS coatings in 3.5wt% NaCl solution. The impedance modulus at a frequency of 0.01 Hz ($|Z|_{f=0.01\ Hz}$) for both coatings is significantly higher than that of the bare Mg alloy (Fig. 10(a)). The $|Z|_{f=0.01\ Hz}$ values for LDH-W and LDH-W/PFDTMS coatings are 8.64 × 10^4 and 2.20 × 10^7 Ω·cm^2, respectively, which are two and five orders of magnitude higher than that of the bare Mg alloy (2.18 × 10^2 Ω·cm^2). Bode phase angle plots corresponding to the different coatings are shown in Fig. 10(b), where the phase angle for the LDH-W/PFDTMS coating at a frequency of 10^5 Hz is approximately −80°. By contrast, these values for the bare Mg alloy and the LDH-W coating are close to 0°, confirming the superior corrosion resistance of the LDH-W/PFDTMS coating. The electrochemical para-

Table 3. Fitted Tafel parameters for LDH-W/PFDTMS-*x* coatings

Samples (LDH-W/PFDTMS-*x*)	E_{corr} / mV	j_{corr} / (10^{-9} A·cm^{-2})	β_a / (mV·dec^{-1})	$-\beta_c$ / (mV·dec^{-1})
12 h	−509	3.4	205	291
18 h	−452	2.03	265	325
24 h	−338	1.86	293	346
30 h	−376	1.96	284	339

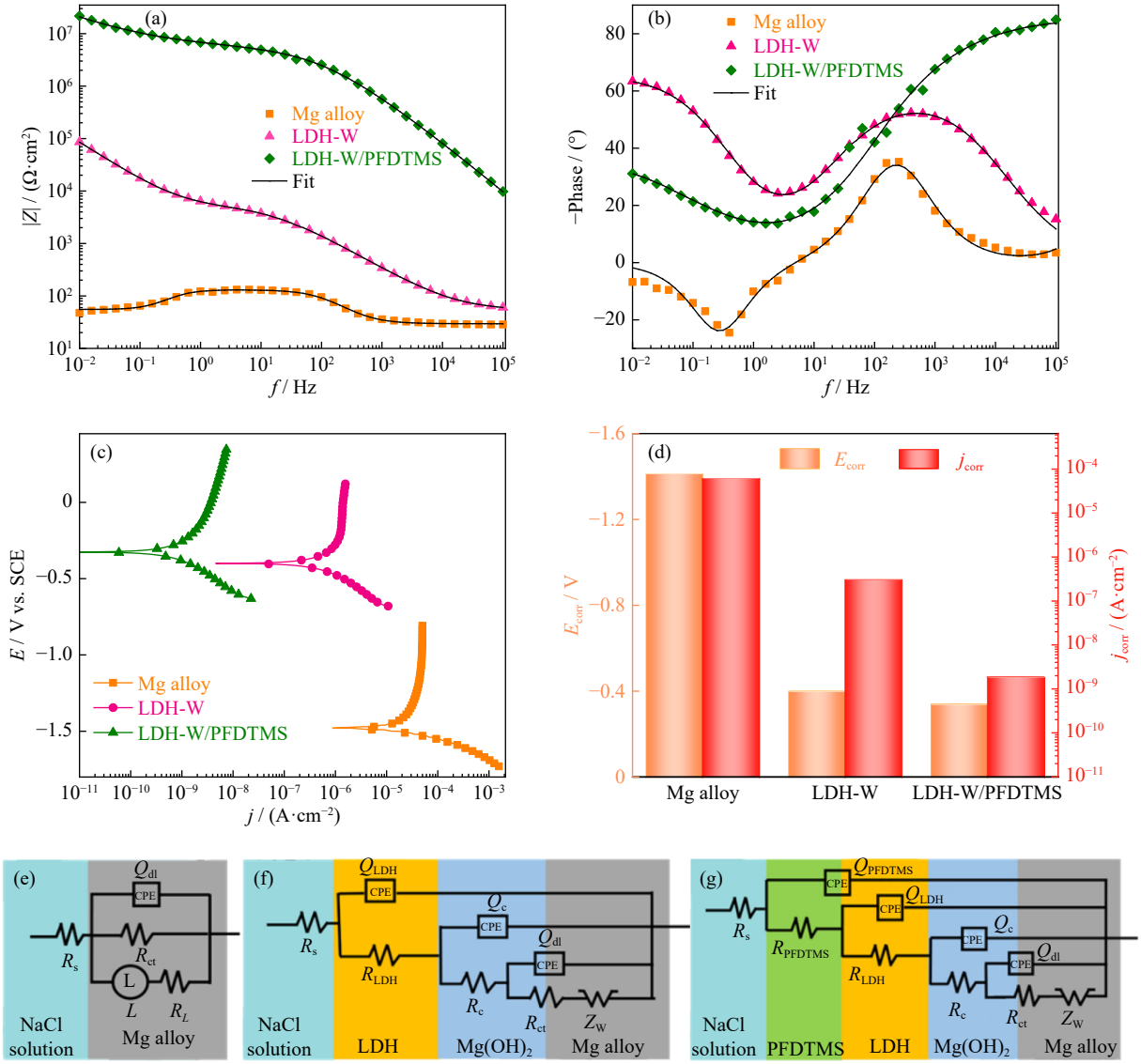

Fig. 10. EIS spectra and Tafel curves of bare Mg alloy, LDH-W, and LDH-W/PFDTMS samples in 3.5wt% NaCl solutions: (a) Bode magnitude diagrams; (b) Bode phase diagrams; (c) Tafel curves; (d) corresponding histograms for E_{corr} and j_{corr} values. Equivalent circuit models for (e) Mg alloy, (f) LDH-W, and (g) LDH-W/PFDTMS coatings.

meters obtained by fitting the experimental data using an EC model (Fig. 10(e)–(g)) are listed in Table 4. The EC model's electrochemical components include R_s, representing the solution resistance, L and R_L, denoting the inductance and resistance associated with the relaxation process induced by corrosion products on the Mg alloy surface [53]; Y_{LDH} and R_{LDH} represent the constant phase element (CPE) and resistance of the LDH-W coating, respectively; Y_c and R_c represent the CPE and resistance of the inner $Mg(OH)_2$ layer, respectively; Y_{dl} and R_{ct} represent the electric double layer's CPE and charge transfer resistance, respectively, while the Z_W represents the Warburg diffusion resistance [54]; R_{PFDTMS} and Y_{PFDTMS}, as shown in Fig. 10(f), represent the resistance and CPE of the PFDTMS layer, respectively. The R_{ct} value of the bare Mg alloy is only 125 Ω·cm^2, which increased by 319 times to 39.9 kΩ·cm^2 for the LDH-W coating and by 14.4 × 10^4 times to 18.0 MΩ·cm^2 for the LDH-W/PFDTMS coating (Table 4). This indicates a significant enhancement in the corrosion protection of the PFDTMS-modified composite coating compared to the pure LDH-W coating.

Table 4. Fitted EIS parameters for Mg alloys, LDH-W, and LDH-W/PFDTMS coatings

Samples	$\lvert Z\rvert_{f=0.01\ Hz}$ / (Ω·cm^2)	R_s / (Ω·cm^2)	Y_{PFDTMS} / (10^{-9} S·s^n·cm^{-2})	R_{PFDTMS} / (kΩ·cm^2)	Y_{LDH} / (10^{-9} S·s^n·cm^{-2})	R_{LDH} / (kΩ·cm^2)	Y_c / (10^{-9} S·s^n·cm^{-2})	R_c / (kΩ·cm^2)	Z_W / (10^{-5} S·s$^{0.5}$·cm^{-2})	Y_{dl} / (10^{-9} S·s^n·cm^{-2})	R_{ct} / (kΩ·cm^2)	χ^2 / 10^{-3}
Mg alloy	2.18 × 10^2	24.5	—	—	—	—	—	—	—	380400	0.125	7.5
LDH-W	8.64 × 10^4	40.1	—	—	5820	5.50	4950	4.30	9.82	142500	39.9	2.40
LDH-W/PFDTMS	2.20 × 10^7	5.6	5.73	3750	3.57	5800	9.74	3500	8.7	5.83	18000	1.8

Fig. 10(c) shows the Tafel curves of Mg alloy, LDH-W, and LDH-W/PFDTMS coatings in 3.5wt% NaCl solution. The corresponding E_{corr} and j_{corr} for the Mg alloy and the different coatings are listed in Table 5. The j_{corr} of LDH-W and LDH-W/PFDTMS coatings are significantly lower, while the E_{corr} are notably higher than those of the bare Mg alloy. The E_{corr} for the Mg alloy is −1410 mV; it improves to −400 mV for the LDH-W coating and is positively shifted to −338 mV for the LDH-W/PFDTMS coating. The j_{corr} is 6.0 × 10^{-5} A·cm^{-2} for the Mg alloy and decreases by two orders of magnitude to 3.03 × 10^{-7} A·cm^{-2} for the LDH-W coating. Following PFDTMS treatment, the j_{corr} of the LDH-W/PFDTMS coating decreases to 1.86 × 10^{-9} A·cm^{-2}, which is four and two orders of magnitude lower than that of Mg alloy and LDH-W coating, respectively. The LDH-W/PFDTMS coating exhibits the lowest j_{corr} and the most positive E_{corr}, demonstrating the outstanding corrosion protection of the developed superhydrophobic composite coating, which is consistent with the EIS findings. Compared with the LDH-W coating, the LDH-W/PFDTMS contains only a nanometer-thick polysiloxane film, indicating that the improvement in corrosion resistance is mainly attributed to its high superhydrophobicity and water repellency.

The corrosion resistance of the coatings was also evaluated by salt spray test. Fig. 11 displays the optical images of the LDH, LDH-W, and LDH-W/PFDTMS coatings after exposure to a salt spray environment at different times. Several obvious corrosion cavities appear at the surface of the LDH coating after just 1 d of exposure. By contrast, small visual corrosion pits begin to form on the surface of the LDH-W coating after 10 d of exposure, with the diameters of these pits becoming larger as exposure time increases. The higher concentration of NaCl solution and elevated temperatures used in the salt spray test accelerate the corrosion rate of the LDH-W coating in the salt spray environment, compared to the immersion test. Compared with the LDH and LDH-W coatings, the superhydrophobic LDH-W/PFDTMS coating shows no visible corrosion pits even after 16 d of salt spray exposure, demonstrating its significantly enhanced corrosion protection of the composite coating for the Mg alloy.

Table 5. Fitted Tafel parameters for Mg alloys, LDH-W, and LDH-W/PFDTMS coatings

Samples	E_{corr} / mV	j_{corr} / (A·cm^{-2})	$-\beta_c$ / (mV·dec^{-1})
Mg alloy	−1410	6.0 × 10^{-5}	87
LDH-W	−400	3.03 × 10^{-7}	213
LDH-W/PFDTMS	−338	1.86 × 10^{-9}	340

Fig. 12 shows the EIS spectra of LDH-W and LDH-W/PFDTMS coatings after being immersed in neutral aqueous solution for different durations to investigate their long-lasting protective capabilities. The fitted parameters by the EC model are listed in Table 6. During immersion, the two coatings' $\lvert Z\rvert_{f=0.01\ Hz}$ values decreased as the immersion time increased. After 15 d of immersion, the R_{ct} of the LDH-W coating decreased slightly by 3.65 kΩ·cm^2 from the initial 39.9 to 36.25 kΩ·cm^2, indicating the stable long-term corrosion resistance of the LDH-W coating, as shown in Fig. 12(a). Conversely, the R_{ct} of the LDH-W/PFDTMS coating decreased evidently from the initial 18.0 to 12.5 MΩ·cm^2 (Fig. 12(c)). Nonetheless, the R_{ct} of the composite coating remained significantly high, approximately 345 times that of the LDH-W coating after 15 d of exposure and much higher than that of the newly prepared LDH-W coating. In addition, the phase angles of the LDH-W/PFDTMS coatings at high frequencies are maintained at approximately −80° (Fig. 12(b) and (d)), confirming the coating's excellent long-term corrosion protection of Mg alloy. The changes in the surface microstructure of the LDH-W/PFDTMS coating after 15 d of immersion were observed using SEM (Fig. 13). The SEM images reveal that the surface morphology of the LDH-W/PFDTMS sample did not change evidently, and the typical nanosheet structure of the LDH was still maintained after 15 d of immersion. These findings underscore the exceptional chemical stability of the superhydrophobic coating.

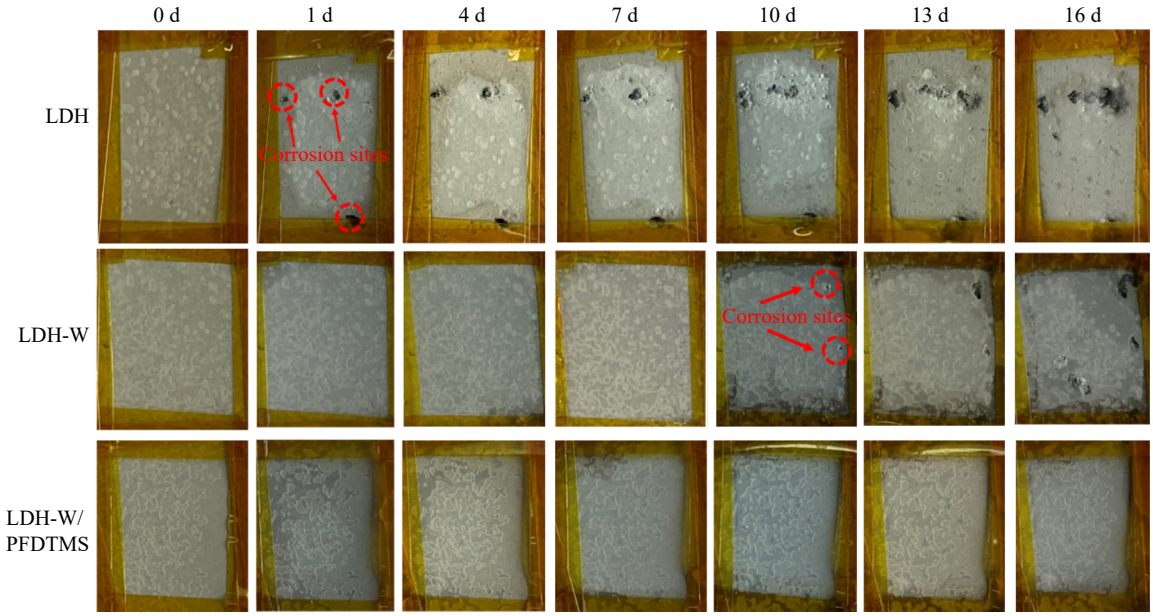

Fig. 11. Optical images of LDH, LDH-W, and LDH-W/PFDTMS coatings after exposure to salt spray environment for different durations.

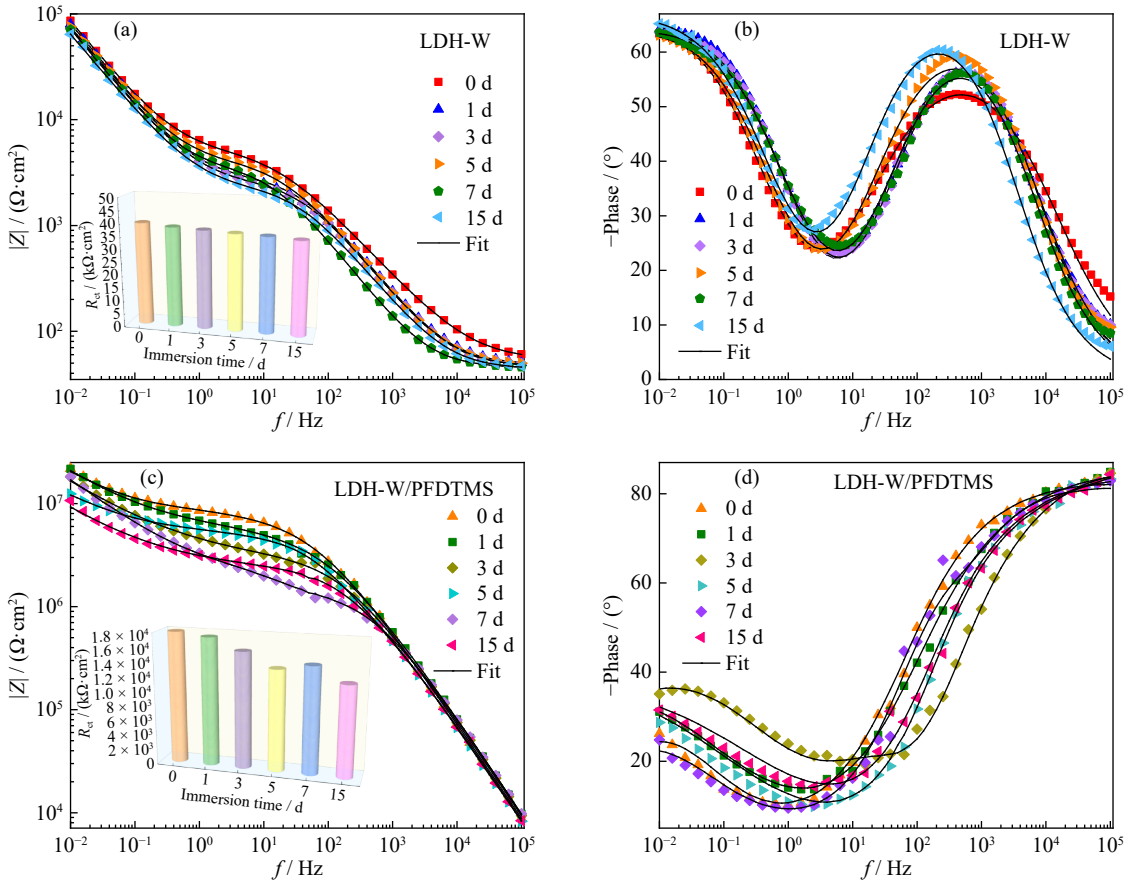

Fig. 12. Bode diagrams of (a, b) LDH-W and (c, d) LDH-W/PFDTMS coatings after exposure to 3.5wt% NaCl solution for different days.

The superior corrosion protection capability of LDH-W/PFDTMS composite coatings mainly stems from the water repellency of the superhydrophobic surface, the physical barrier effect, the entrapment of corrosive ions, and the corrosion inhibition owing to the release of inhibitors from the LDH-W layer. The corrosion protection of the LDH-W coating is mainly attributed to the physical barrier properties and ability to capture corrosive anions (such as Cl^-) and release corrosion inhibitors through ion exchange function. Compared with the pure LDH-W coating, the water repellency provided by the uppermost polysiloxane layer, which has low surface energy in the LDH-W/PFDTMS coating, is crucial

Table 6. Fitted EIS parameters of LDH-W and LDH-W/PFDTMS coatings after exposure to 3.5wt% NaCl solution for different days

Samples	Immersion time / d	R_s / ($\Omega\cdot cm^2$)	Y_{PFDTMS} / (10^{-9} $S\cdot s^n\cdot cm^{-2}$)	R_{PFDTMS} / ($k\Omega\cdot cm^2$)	Y_{LDH} / (10^{-9} $S\cdot s^n\cdot cm^{-2}$)	R_{LDH} / ($k\Omega\cdot cm^2$)	Y_c / (10^{-9} $S\cdot s^n\cdot cm^{-2}$)	R_c / ($k\Omega\cdot cm^2$)	Z_W / (10^{-5} $S\cdot s^{0.5}\cdot cm^{-2}$)	Y_{dl} / (10^{-9} $S\cdot s^n\cdot cm^{-2}$)	R_{ct} / ($k\Omega\cdot cm^2$)	χ^2 / 10^{-3}
LDH-W	0	40.1	—	—	5820	5.50	4950	4.30	9.82	142500	39.9	2.40
	1	44.8	—	—	5810	2.98	5350	3.76	8.02	151300	38.87	3.36
	3	45.2	—	—	5700	3.21	5780	3.21	6.62	15500	38.28	1.45
	5	43.6	—	—	6960	2.4	5860	3.01	6.82	154500	37.57	1.49
	7	45.7	—	—	5540	3.68	5140	3.85	12.17	135300	37.08	1.72
	15	42.3	—	—	5865	3.58	5320	3.53	11.83	133500	36.25	2.78
LDH-W/ PFDTMS	0	5.6	5.73	3750	3.57	5800	9.74	3500	8.7	5.83	18000	1.80
	1	3	5.77	3660	3.59	5670	9.84	3437	8.64	6.74	17500	1.93
	3	1.8	5.96	3480	3.82	5570	9.92	3397	7.86	6.98	15890	1.22
	5	2.8	6.16	3371	3.91	5452	9.96	3280	7.55	8.78	13870	5.10
	7	1.5	5.93	3301	3.87	5490	9.95	3359	6.94	10.65	14620	1.37
	15	2.3	6.61	3008	4.11	5100	9.99	3256	6.24	12.33	12540	1.89

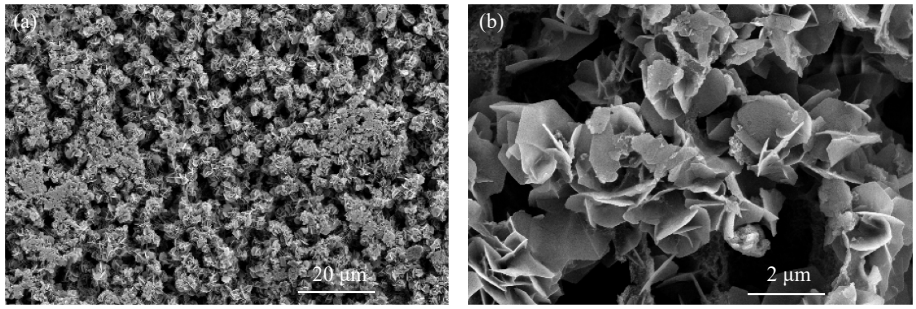

Fig. 13. SEM image of the LDH-W/PFDTMS coating after immersion for 15 d.

for improving corrosion resistance. The aqueous corrosive medium cannot fully impregnate the PFDTMS-modified LDH-W nanosheets. These micro- and nanoscale gaps among the LDH-W nanosheets can trap air, forming an "air cushion" that reduces the contact area between the corrosive medium and the film. This decreased contact area impedes the infiltration of the corrosive medium into the substrate, greatly improving the corrosion resistance of the composite coating.

4. Conclusion

The superhydrophobic and corrosion-resistant LDH-W/PFDTMS composite coating consisting of tungstate-intercalated LDH primer and polysiloxane top layer was successfully prepared on the surface of Mg alloy at low temperatures and under atmospheric pressure. The composite coating exhibited remarkable superhydrophobicity, self-cleaning capabilities against several common aqueous beverages, and outstanding long-lasting corrosion resistance in neutral solutions for the Mg alloy. The superior corrosion protection of the composite coating can be attributed to the water repellency of the PFDTMS outer layer and the physical barrier it creates, its ability to trap corrosive anions such as chloride, and the corrosion inhibition provided by the inhibitors released by the anion exchange process of the LDH phase. These results demonstrated that constructing superhydrophobic and corrosion-resistant LDH-based composite coatings under mild reaction conditions is feasible and beneficial for the large-scale industrial application of LDH coatings in surface treatments for Mg alloys.

Acknowledgements

This work was financially supported by the National Natural Science Foundation of China (No. 52271073), the Sichuan Provincial Natural Science Foundation for Distinguished Young Scholars, China (No. 2024NSFJQ0034), and the Innovation Team Funds of China West Normal University (No. KCXTD2024–1).

Conflict of Interest

The authors declare that there is no conflict of interest.

References

[1] P. Pesode and S. Barve, Additive manufacturing of magnesium alloys and its biocompatibility, *Bioprinting*, 36(2023), art. No. e00318.

[2] Y.B. Zhao, J. Bai, F. Xue, *et al*., Smart self-healing coatings on biomedical magnesium alloys: A review, *Smart Mater. Manuf.*, 1(2023), art. No. 100022.

[3] M.F. Qi, L.Y. Wei, Y.Z. Xu, *et al*, Effect of trace yttrium on the microstructure, mechanical property and corrosion behavior of

homogenized Mg–2Zn–0.1Mn–0.3Ca–*x*Y biological magnesium alloy, *Int. J. Miner. Metall. Mater.*, 29(2022), No. 9, p. 1746.

[4] W. Zai, X.R. Zhang, Y.C. Su, H.C. Man, G.Y. Li, and J.S. Lian, Comparison of corrosion resistance and biocompatibility of magnesium phosphate (MgP), zinc phosphate (ZnP) and calcium phosphate (CaP) conversion coatings on Mg alloy, *Surf. Coat. Technol.*, 397(2020), art. No. 125919.

[5] G.Q. Duan, L.X. Yang, S.J. Liao, *et al*, Designing for the chemical conversion coating with high corrosion resistance and low electrical contact resistance on AZ91D magnesium alloy, *Corros. Sci.*, 135(2018), p. 197.

[6] C.Y. Zhang, Y.Y. Chen, B.X. Yu, *et al*, Effects of nucleation pretreatment on corrosion resistance of conversion coating on magnesium alloy Mg–10Gd–3Y–0.4Zr, *Corros. Commun.*, 10(2023), p. 69.

[7] X.M. Wang, G.J. Lu, L.Y. Cui, *et al*, *In vitro* degradation and biocompatibility of vitamin C loaded Ca–P coating on a magnesium alloy for bioimplant applications, *Corros. Commun.*, 6(2022), p. 16.

[8] D. Saran, A. Kumar, S. Bathula, D. Klaumünzer, and K.K. Sahu, Review on the phosphate-based conversion coatings of magnesium and its alloys, *Int. J. Miner. Metall. Mater.*, 29(2022), No. 7, p. 1435.

[9] G.L. Yang, Y.J. Ouyang, Z.H. Xie, Y. Liu, W.X. Dai, and L. Wu, Nickel interlayer enables indirect corrosion protection of magnesium alloy by photoelectrochemical cathodic protection, *Appl. Surf. Sci.*, 558(2021), art. No. 149840.

[10] I. Fatima, O. Fayyaz, M.M. Yusuf, A. Al Ashraf, and R.A. Shakoor, Enhanced electrochemical and mechanical performance of BN reinforced Ni–P based nanocomposite coatings, *Diam. Relat. Mater.*, 130(2022), art. No. 109454.

[11] M.H. Sliem, O. Fayyaz, R.A. Shakoor, *et al*, The influence of different preparation methods on the erosion behavior of NiP–ZrO_2 nanocomposite coating, *Tribol. Int.*, 178(2023), art. No. 108014.

[12] A. Fattah-alhosseini and R. Chaharmahali, Impressive strides in amelioration of corrosion behavior of Mg-based alloys through the PEO process combined with surface laser process: A review, *J. Magnesium Alloys*, 11(2023), No. 12, p. 4390.

[13] R.J. Liu, Y. Liu, Q.W. Yong, Z.H. Xie, L. Wu, and C.J. Zhong, Highly corrosion-resistant ZIF-8-integrated micro-arc oxidation coating on Mg alloy, *Surf. Coat. Technol.*, 463(2023), art. No. 129505.

[14] X.Y. Yang, X.P. Lu, Y.X. Zhou, Y.F. Xie, J.J. Yang, and F.H. Wang, Formation of protective conversion coating on Mg surface by inorganic inhibitor, *Corros. Sci.*, 215(2023), art. No. 111044.

[15] Q.Q. Chen, X.P. Lu, M. Serdechnova, *et al*, Formation of self-healing PEO coatings on AM50 Mg by *in situ* incorporation of zeolite micro-container, *Corros. Sci.*, 209(2022), art. No. 110785.

[16] S.Y. Jin, X.C. Ma, R.Z. Wu, *et al*, Effect of carbonate additive on the microstructure and corrosion resistance of plasma electrolytic oxidation coating on Mg–9Li–3Al alloy, *Int. J. Miner. Metall. Mater.*, 29(2022), No. 7, p. 1453.

[17] R.J. Liu, D. Xu, Y. Liu, L. Wu, Q.W. Yong, and Z.H. Xie, Enhanced corrosion protection for MAO coating on magnesium alloy by the synergism of LDH doping with deposition of 8HQ inhibitor film, *Ceram. Int.*, 49(2023), No. 18, p. 30039.

[18] Y. Wang, Z.P. Gu, J. Liu, *et al*, An organic/inorganic composite multi-layer coating to improve the corrosion resistance of AZ31B Mg alloy, *Surf. Coat. Technol.*, 360(2019), p. 276.

[19] J.Y. Yang, Y.B. Zhao, J.W. Dai, *et al*, Fabrication and growth mechanism of multilayered hydroxyapatite/organic composite coatings on the WE43 magnesium alloy, *Surf. Coat. Technol.*, 452(2023), art. No. 129125.

[20] Y.J. Tarzanagh, D. Seifzadeh, and R. Samadianfard, Combining the 8-hydroxyquinoline intercalated layered double hydroxide film and sol–gel coating for active corrosion protection of the magnesium alloy, *Int. J. Miner. Metall. Mater.*, 29(2022), No. 3, p. 536.

[21] K. Abdi-Alghanab, D. Seifzadeh, Z. Rajabalizadeh, and A. Habibi-Yangjeh, High corrosion protection performance of the LDH/Ni–P composite coating on AM60B magnesium alloy, *Surf. Coat. Technol.*, 397(2020), art. No. 125979.

[22] G.Z. Shen, L.Y. Zhang, Z.W. Gu, *et al*, Zinc aluminum-layered double hydroxide(LDH)–graphene oxide(GO) lubricating and corrosion-resistant composite coating on the surface of magnesium alloy, *Surf. Coat. Technol.*, 437(2022), art. No. 128354.

[23] F. Peng, D.D. Zhang, X.Y. Liu, and Y. Zhang, Recent progress in superhydrophobic coating on Mg alloys: A general review, *J. Magnesium Alloys*, 9(2021), No. 5, p. 1471.

[24] Z.W. Song, Z.F. Huang, Z.H. Xie, *et al*, Preparation and corrosion resistance of robust superhydrophobic nickel-based coating, *Surf. Technol*, 52(2023), No.12, p. 379.

[25] C.C. Li, T.T. Liang, R.N. Ma, *et al*, Superhydrophobic surface containing cerium salt and organosilane for corrosion protection of galvanized steel, *J. Alloys Compd.*, 825(2020), art. No. 153921.

[26] S.J. Song, H. Yan, M. Cai, *et al*, Superhydrophobic composite coating for reliable corrosion protection of Mg alloy, *Mater. Des.*, 215(2022), art. No. 110433.

[27] S.J. Zhang, D.L. Cao, L.K. Xu, J.K. Tang, R.Q. Meng, and H.D. Li, Corrosion resistance of a superhydrophobic dodecyltrimethoxysilane coating on magnesium hydroxide-pretreated magnesium alloy AZ31 by electrodeposition, *Colloids Surf. A*, 625(2021), art. No. 126914.

[28] R. Fang, R.J. Liu, Z.H. Xie, L. Wu, Y.J. Ouyang, and M.Q. Li, Corrosion-resistant and superhydrophobic nickel–phosphorus/nickel/PFDTMS triple-layer coating on magnesium alloy, *Surf. Coat. Technol.*, 432(2022), art. No. 128054.

[29] Y.Q. Li, Y.J. Ouyang, R. Fang, *et al*, A nickel-underlayer/LDH-midlayer/siloxane-toplayer composite coating for inhibiting galvanic corrosion between Ni layer and Mg alloy, *Chem. Eng. J.*, 430(2022), art. No. 132776.

[30] X.G. Wang, L.C. Yan, K.W. Gao, P.C. Li, and J.J. Hao, Enhancing the corrosion resistance of ZnAl–LDHs films on AZ91D magnesium alloys by designing surface roughness, *Coatings*, 13(2023), No. 4, art. No. 724.

[31] L.F. Hou, Y.L. Li, J.L. Sun, S.H. Zhang, H. Wei, and Y.H. Wei, Enhancement corrosion resistance of MgAl layered double hydroxides films by anion-exchange mechanism on magnesium alloys, *Appl. Surf. Sci.*, 487(2019), p. 101.

[32] T. Shulha, M. Serdechnova, S.V. Lamaka, *et al*, Corrosion inhibitors intercalated into layered double hydroxides prepared *in situ* on AZ91 magnesium alloys: Structure and protection ability, *ACS Appl. Mater. Interfaces*, 15(2023), No. 4, p. 6098.

[33] R.R. Li, W.Q. Liu, H.B. Liu, *et al*, Dual active sites of Ni and $FeNi_3$ constructed from layered double hydroxides for one-pot hydrogenation of furfural to tetrahydrofurfuryl alcohol, *Ind. Eng. Chem. Res.*, 62(2023), No. 50, p. 21631.

[34] Z.W. Jiang, J.N. Wu, X.R. Liu, *et al*, Facile synthesis of MgAl layered double hydroxides by a co-precipitation method for efficient nitrate removal from water: Kinetics and mechanisms, *New J. Chem.*, 45(2021), No. 32, p. 14580.

[35] C.D. Ding, Y. Tai, D. Wang, L.H. Tan, and J.J. Fu, Superhydrophobic composite coating with active corrosion resistance for AZ31B magnesium alloy protection, *Chem. Eng. J.*, 357(2019), p. 518.

[36] K.Y. Cao, Z.X. Yu, L.J. Zhu, *et al*, Fabrication of superhydrophobic layered double hydroxide composites to enhance the corrosion-resistant performances of epoxy coatings on Mg alloy, *Surf. Coat. Technol.*, 407(2021), art. No. 126763.

[37] Q.S. Yao, F. Zhang, L. Song, *et al*, Corrosion resistance of a ceria/polymethyltrimethoxysilane modified Mg–Al-layered double hydroxide on AZ31 magnesium alloy, *J. Alloys Compd.*, 764(2018), p. 913.
[38] R.H. Temperton, J.N. O'Shea, and D.J. Scurr, On the suitability of high vacuum electrospray deposition for the fabrication of molecular electronic devices, *Chem. Phys. Lett.*, 682(2017), p. 15.
[39] T.Y. Kim, D.S. Park, Y. Choi, J. Baek, J.R. Park, and J. Yi, Preparation and characterization of mesoporous Zr–WO_x/SiO_2 catalysts for the esterification of 1-butanol with acetic acid, *J. Mater. Chem.*, 22(2012), No. 19, p. 10021.
[40] X. Li, J.X. Yang, J.J. Wang, X.J. Chang, J.L. Xu, and Z.H. Wu, A stable super-amphiphilic surface created from superhydrophobic silica/epoxy coating by low-temperature plasma-treatment, *Surf. Eng.*, 37(2021), No. 10, p. 1282.
[41] L.J. Yang, X.Q. Cheng, Y.L. Ma, *et al*, Changing of SEI film and electrochemical properties about MCMB electrodes during long-term charge/discharge cycles, *J. Electrochem. Soc.*, 160(2013), No. 11, p. A2093.
[42] Y. Zhang, X. He, J. Ouyang, and H.M. Yang, Palladium nanoparticles deposited on silanized halloysite nanotubes: Synthesis, characterization and enhanced catalytic property, *Sci. Rep.*, 3(2013), art. No. 2948.
[43] Y.J. Ouyang, Z.F. Huang, R. Fang, L. Wu, Q.W. Yong, and Z.H. Xie, Silica nanoparticles enhanced polysiloxane-modified nickel-based coatings on Mg alloy for robust superhydrophobicity and high corrosion resistance, *Surf. Coat. Technol.*, 450(2022), art. No. 128995.
[44] H.D. Liu, D.Y. Liu, P.H. Li, Y.J. Zeng, and H.Y. Jin, Direct observation of the wetting state of Cassie and Wenzel, *Mater. Lett.*, 340(2023), art. No. 134182.
[45] G. Whyman, E. Bormashenko, and T. Stein, The rigorous derivation of Young, Cassie–Baxter and Wenzel equations and the analysis of the contact angle hysteresis phenomenon, *Chem. Phys. Lett.*, 450(2008), No. 4-6, p. 355.
[46] X. Zhang, W.Z. Zhu, G.J. He, P.Y. Zhang, Z.J. Zhang, and I.P. Parkin, Flexible and mechanically robust superhydrophobic silicone surfaces with stable Cassie–Baxter state, *J. Mater. Chem. A*, 4(2016), No. 37, p. 14180.
[47] U. Cengiz and C. Elif Cansoy, Applicability of Cassie–Baxter equation for superhydrophobic fluoropolymer–silica composite films, *Appl. Surf. Sci.*, 335(2015), p. 99.
[48] T.F. Xiang, M. Zhang, H.R. Sadig, *et al*, Slippery liquid-infused porous surface for corrosion protection with self-healing property, *Chem. Eng. J.*, 345(2018), p. 147.
[49] Y. Shu, F. Peng, Z.H. Xie, *et al*, Well-oriented magnesium hydroxide nanoplatelets coating with high corrosion resistance and osteogenesis on magnesium alloy, *J. Magnesium Alloys*, (2023)
[50] X. Wang, C. Jing, Y.X. Chen, *et al*, Active corrosion protection of super-hydrophobic corrosion inhibitor intercalated Mg–Al layered double hydroxide coating on AZ31 magnesium alloy, *J. Magnesium Alloys*, 8(2020), No. 1, p. 291.
[51] N. Li, N. Ling, H.Y. Fan, L. Wang, and J.L. Zhang, Self-healing and superhydrophobic dual-function composite coating for active protection of magnesium alloys, *Surf. Coat. Technol.*, 454(2023), art. No. 129146.
[52] Z.F. Huang, Q.W. Yong, and Z.H. Xie, Stearic acid modified porous nickel-based coating on magnesium alloy AZ31 for high superhydrophobicity and corrosion resistance, *Corros. Commun.*, 10(2023), p. 38.
[53] Q. Li, S.Q. Xu, J.Y. Hu, S.Y. Zhang, X.K. Zhong, and X.K. Yang, The effects to the structure and electrochemical behavior of zinc phosphate conversion coatings with ethanolamine on magnesium alloy AZ91D, *Electrochim. Acta*, 55(2010), No. 3, p. 887.
[54] T. Hu, Y.J. Ouyang, Z.H. Xie, and L. Wu, One-pot scalable *in situ* growth of highly corrosion-resistant MgAl–LDH/MBT composite coating on magnesium alloy under mild conditions, *J. Mater. Sci. Technol.*, 92(2021), p. 225.